ACS APPLIED MATERIALS & INTERFACES

www.acsami.org

Research Article

Atomic Dispersion and Surface Enrichment of Palladium in Nitrogen-Doped Porous Carbon Cages Lead to High-Performance Electrocatalytic Reduction of Oxygen

Qiming Liu, Yi Peng, Qiaoxia Li, Ting He, David Morris, Forrest Nichols, Rene Mercado, Peng Zhang, and Shaowei Chen*

Cite This: *ACS Appl. Mater. Interfaces* 2020, 12, 17641−17650

Read Online

ACCESS | Metrics & More | Article Recommendations | Supporting Information

ABSTRACT: Metal−nitrogen−carbon (MNC) nanocomposites have been hailed as promising and efficient electrocatalysts toward oxygen reduction reaction (ORR), due to the formation of MN_x coordination moieties. However, MNC hybrids are mostly prepared by pyrolysis of organic precursors along with select metal salts, where part of the MN_x sites are inevitably buried in the carbon matrix. This limited accessibility compromises the electrocatalytic performance. Herein, we describe a wet-impregnation procedure by facile thermal refluxing, whereby palladium is atomically dispersed and enriched onto the surface of hollow, nitrogen-doped carbon cages (HNC) forming Pd−N coordination bonds. The obtained Pd-HNC nanocomposites exhibit an ORR activity in alkaline media markedly higher than that of metallic Pd nanoparticles, and the best sample even outperforms commercial Pt/C and relevant Pd-based catalysts reported in the literature. The results suggest that atomic dispersion and surface enrichment of palladium in a carbon matrix may serve as an effective strategy in the fabrication of high-performance ORR electrocatalysts.

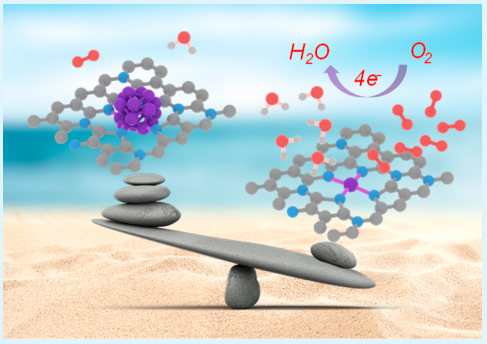

KEYWORDS: *ZIF-8, carbon cage, thermal refluxing, wet impregnation, palladium single atom, oxygen reduction reaction*

INTRODUCTION

Oxygen reduction reaction (ORR) is a critical process at the cathodes of fuel cells and metal−air batteries, where the sluggish electron-transfer kinetics has been recognized as a major bottleneck that limits the device performance.[1−3] Platinum-based nanoparticles have been used as the catalysts of choice toward ORR.[4−7] Palladium also exhibits apparent ORR activity. In the well-known "volcano plot", bulk palladium shows a moderate oxygen adsorption energy, yet it remains too strong as compared to that of platinum.[2,8] Therefore, a range of structural variables have been examined to manipulate the electronic structure of Pd so as to further enhance the ORR activity, such as nanoparticle size and shape,[9−12] alloying,[13,14] and interfacial interactions with substrate supports/capping ligands.[15−18] Atomic dispersion of Pd into a nitrogen-doped carbon matrix forming PdN_x moieties represents a new strategy to reach the apex of the "volcano plot".[15,19] In such single atom catalysts (SACs),[20,21] the catalytic activity, durability, and selectivity can be enhanced by the unique metal−support interfacial interactions as compared to their corresponding nanoparticle or bulk counterparts.[22−31]

SACs are prepared predominantly by pyrolysis. For instance, Zhou et al.[32] prepared Pd single atoms by pyrolysis of N-doped graphene with Pd salts at 800 °C. The obtained sample showed a 93.5% selectivity in the semi-hydrogenation of acetylene to ethylene—a performance superior to that (56%) with Pd nanoparticles. A similar behavior was also observed by Wei et al.,[33] where Pd nanoparticles encapsulated by zeolitic imidazole frameworks 8 (ZIF-8) were transformed into Pd single atoms by pyrolysis at 900 °C, and the resultant sample showed a better catalytic selectivity (93.4%) than Pd nanoparticles (71.8%). In these studies, the catalytic activity was ascribed to the formation of PdN_x structures. However, high-temperature pyrolysis inevitably renders part of the resulting PdN_x moieties to be buried within the carbon matrix and become inaccessible, which compromises the overall catalytic performance.[23,24,34,35] This issue can be effectively mitigated by wet impregnation, whereby metal centers are immobilized mostly onto the surface of the substrate support, and the surface enrichment facilitates accessibility of the catalytic centers. For instance, Podyacheva et al.[36] used N-doped carbon nanotubes to capture Pd single atoms (0.2−0.5 wt %) in acetone, followed by H_2 reduction. The PdN_x active sites exhibited a higher turnover frequency

Received: February 21, 2020
Accepted: March 23, 2020
Published: March 23, 2020

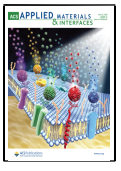

https://dx.doi.org/10.1021/acsami.0c03415
ACS Appl. Mater. Interfaces 2020, 12, 17641−17650

(TOF, 0.081 s^{-1}) than Pd particles (~0.06 s^{-1}) toward formic acid decomposition at 125 °C. Bulushev et al.[37] soaked N-doped mesoporous carbon into a palladium salt solution to produce single Pd active sites (~1 wt %). The sample that consisted of isolated Pd(II) cations demonstrated a TOF over 3 times higher than that of commercial Pd powders toward hydrogen production from formic acid. Nevertheless, in these earlier studies, only a small number of PdN_x active sites were formed because of the low concentration of N dopants in the carbon matrices, which limited the eventual catalytic performance.

It should be noted that studies of palladium SACs for ORR have been scarce, although atomic palladium species are known to exhibit more optimal binding for oxygen intermediates than the bulk metal of palladium, and drastically enhanced mass activity.[19,38−40] For instance, Passaponti et al.[38] deposited N-coordinated Pd(II) macrocyclic complexes on carbon nanotubes and observed apparent ORR activity with an onset potential (E_{onset}) of +0.95 V vs RHE and a half-wave potential ($E_{1/2}$) of +0.86 V, markedly better than that of a polycrystalline Pt electrode (E_{onset} = +0.91 V and $E_{1/2}$ = +0.82 V). Xiang et al.[39] reported that Pd single atoms supported on manganese(IV) oxide−carbon nanotube (MnO_2−CNT) nanocomposites exhibited an optimized binding strength to ORR intermediates, with a much higher Pd mass activity (484 A g^{-1} at +0.90 V) than that of commercial Pd/C (20 A g^{-1}). Arrigo et al.[19] also observed that PdN_x in Pd-doped carbon nanotubes improved the ORR activity with an E_{onset} of +0.88 V, in comparison to only +0.75 V with metallic Pd nanoparticles. Yet, the ORR performance of these palladium-based catalysts remains subpar as compared to that of state-of-the-art Pt/C.

Herein, we describe a wet-impregnation procedure based on facile thermal refluxing[41,42] to embed Pd metal centers onto the surface of N-doped porous carbon cages (HNC) that were prepared *a prior* pyrolytically from ZIF-8. The resulting Pd-HNC nanocomposites were found to exhibit abundant micro/meso/macropores decorated with pyridinic/pyrrolic nitrogen dopants, which facilitated the chelation of metal ions.[43,44] Because the Pd centers resided mostly on the carbon surface, the electrochemical accessibility was maximal, a critical feature for the optimization of the electrocatalytic (mass) activity. Experimentally, we observe that whereas a small number of Pd nanoparticles were also produced in the samples, the Pd SACs in Pd-HNC played a dominant role in ORR electrocatalysis, and the sample with a saturated Pd loading even outperformed commercial 20% Pt/C with an $E_{1/2}$ that was 40 mV more positive.

EXPERIMENTAL SECTION

Chemicals. 2-Methylimidazole ($CH_3C_3H_2N_2H$, 99%, Acros Organics), tannic acid ($C_{76}H_{52}O_{46}$, certified ACS, Electron Microscopy Sciences), ethylenediaminetetraacetic acid disodium salt dihydrate (EDTA, ACS, Calbiochem), zinc nitrate hexahydrate ($Zn(NO_3)_2{\cdot}6H_2O$, certified ACS, Fisher Chemicals), palladium(II) acetate ($Pd(OAc)_2$, 99.98%, Alfa Aesar), potassium hydroxide (KOH, certified ACS, Fisher Chemicals), potassium thiocyanate (KSCN, Spectrum Chemicals), and Pt/C (20 wt %, Alfa Aesar) were used as received without further purification. Water was supplied from a Barnstead Nanopure water system (18.3 MΩ·cm).

Synthesis of ZIF-8. In a typical synthesis,[45] 1.116 g of $Zn(NO_3)_2{\cdot}6H_2O$ was dissolved in 30 mL of methanol in a vial, and 1.232 g of 2-methylimidazole was dissolved in 30 mL of methanol in another vial. These two solutions were then mixed under sonication for 10 min to form a milky-white solution. The solution was transferred to a 100 mL Teflon-lined stainless-steel autoclave and heated at 120 °C for 2 h, producing a milky precipitate that was collected via centrifugation at 6000 rpm for 5 min, rinsed three times with methanol, and dried under vacuum at 50 °C for 12 h. The obtained product was the ZIF-8 crystals.

Synthesis of Hollow ZIF-8. 80 mg of the as-prepared ZIF-8 crystals was dispersed in 3 mL of Nanopure water under sonication for 20 min, into which was then injected 7 mL of a tannic acid solution (5 mg mL^{-1} in water) under magnetic stirring for 10 min to form an orange solution. After centrifugation, the precipitates were rinsed three times with water and then dried under vacuum at 50 °C, affording hollow ZIF-8.

Synthesis of HNC. HNC was prepared by pyrolysis of hollow ZIF-8. Experimentally, the hollow ZIF-8 powders prepared above were transferred into a ceramic boat, which was then placed into a tube furnace, heated to 900 °C at a ramp rate of 5 °C min^{-1}, and kept at 900 °C for 3 h under a nitrogen atmosphere. The pyrolyzed sample was cooled naturally, which was denoted as HNC.

Synthesis of Pd-HNC. Under sonication for 20 min, 20 mg of HNC was dispersed in 30 mL of acetonitrile in a flask, along with the addition of a certain amount of $Pd(OAc)_2$ (i.e., 1, 2, 5, or 10 mg). The mixture was refluxed at 70 °C for 10 h in an oil bath, before the precipitates were collected by centrifugation and dried under vacuum at 50 °C for 12 h. The resulting samples were termed Pd-HNC_1, Pd-HNC_2, Pd-HNC_5, and Pd-HNC_{10}, respectively.

A control sample PdNP/HNC was prepared by $NaBH_4$ reduction of $Pd(OAc)_2$ in the presence of HNC, where Pd nanoparticles were deposited on the HNC surface. Briefly, 20 mg of HNC was dispersed in 15 mL of acetonitrile with 1.5 mg of $Pd(OAc)_2$ (0.1 mg mL^{-1}) in an ice bath, into which was then injected 250 μL of a freshly prepared $NaBH_4$ solution (7 mg mL^{-1}). The resulting precipitates were centrifuged and dried under vacuum at 50 °C for 12 h.

Characterizations. Transmission electron microscopic (TEM) measurements were performed with a JEOL JEM-2100F electron microscope. X-ray photoelectron spectra (XPS) were acquired with a PHI-5400/XPS instrument with an Al Kα source operated at 350 W and 10^{-9} Torr. X-ray diffraction (XRD) patterns were collected with a Bruker D8 Advance diffractometer with Cu Kα radiation (λ = 0.15418 nm). The specific surface areas of the samples were measured by using Langmuir and Brunauer−Emmett−Teller (BET) methods on a Micromeritics ASAP 2020 porosimetry system at 77.3 K. The adsorption branches of the isotherms were used to obtain the pore width distribution curves by using nonlocal density functional theory (NLDFT). Contents of metal elements in the catalysts were quantified by using inductively coupled plasma optical emission spectroscopy (ICP-OES) on a PerkinElmer Optima instrument. UV−vis absorption spectra were acquired with a PerkinElmer Lambda 35 UV−vis spectrometer.

X-ray Absorption Spectroscopy (XAS). Pd K-edge XAS data were collected at the CLS@APS (Sector 20-BM) beamline at the Advanced Photon Source (7.0 GeV) in Argonne National Laboratory (Chicago, IL). Powdered samples were measured in fluorescence mode simultaneously with a Pd foil reference. All measurements were conducted at room temperature and ambient pressure. Extended X-ray absorption fine structure (EXAFS) data were transformed and normalized into *k*- and *R*-space using the Athena program following conventional procedures.[46] A *k* weighting of 2 was used to obtain all FT-EXAFS spectra. A *k* range of 3.5 to 11.0 $Å^{-1}$ and a *R* range of 1.0 to 3.3 Å were used. Self-consistent multiple-scattering calculations were performed using the FEFF6 program to obtain the scattering amplitudes and phase-shift functions used to fit various scattering paths with the Artemis program. In the fitting of all samples, the E_0 values were correlated together to minimize the number of independent values, allowing reliable fitting results to be obtained.

Electrochemistry. All electrochemical tests were performed with a CHI 710 electrochemical workstation in a conventional three-electrode cell, using a Ag/AgCl (1 M KCl) electrode as the reference electrode, a graphite rod as the counter electrode, and a polished rotating ring (gold) disk (glassy carbon) electrode (RRDE, from Pine Instrument Co.) as the working electrode. The Ag/AgCl electrode

https://dx.doi.org/10.1021/acsami.0c03415
ACS Appl. Mater. Interfaces 2020, 12, 17641−17650

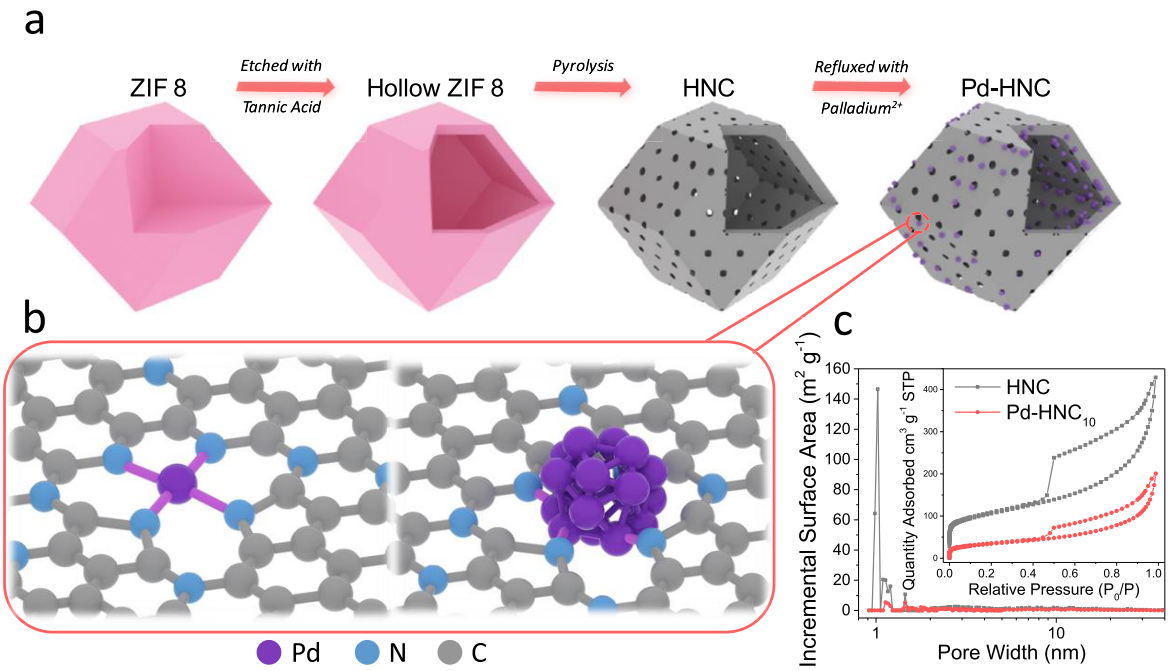

Figure 1. Schematic illustrations of (a) the preparation of Pd-HNC, where (b) both atomically dispersed PdN_x sites and palladium nanoclusters may be formed depending on the initial feed of palladium. (c) Pore size distribution profiles of HNC and Pd-HNC_{10}. Inset is the corresponding nitrogen sorption isotherms.

was calibrated against a reversible hydrogen electrode (RHE), and all potentials in this study were referenced to this RHE. During the ORR tests, the ring potential was set at +1.5 V vs RHE. To prepare the catalyst inks, 2 mg of the samples obtained above was added into 1 mL of an isopropanol/water (3:1 v/v) mixture and 10 μL of a 100 wt % Nafion solution. The suspension was sonicated to form a homogeneous ink. 20 μL of the ink was then drop-cast onto the glassy carbon disk electrode (surface area 0.246 cm^2), dried at room temperature, and coated with 5 μL of a 20 wt % Nafion solution, corresponding to a catalyst loading of 0.162 mg cm^{-2}.

RESULTS AND DISCUSSION

The synthetic procedure of the Pd-HNC samples entails four major steps. As illustrated in Figure 1a, the first step is hydrothermal synthesis of ZIF-8 powders from zinc(II) nitrate and 2-methylimidazole.[47] Tannic acid is then used to etch the inner part of ZIF-8, resulting in the formation of a hollow structure.[48−50] Notably, in comparison to other template-based methods to produce hollow nanostructures,[25,51] chemical etching by tannic acid can not only facilely remove the ZIF-8 inner cores but also retain the pristine shape.[47,52] Subsequent pyrolysis at 900 °C leads to effective carbonization of the hollow ZIF-8 precursor into HNC with abundant nitrogen dopants.[43] During pyrolysis, the volatilization of the zinc compounds within the hollow ZIF-8 leads to the formation of extensive porosity in the carbon matrix. Palladium species are then impregnated onto the HNC surface by thermal refluxing of HNC and palladium(II) acetate, most likely by virtue of the formation of Pd−N bonds, leading to atomic dispersion and surface enrichment of the Pd centers (Figure 1b). Note that a small number of Pd nanoclusters can also be formed at high palladium feeding ratios.

Four Pd-HNC samples (Pd-HNC_1, Pd-HNC_2, Pd-HNC_5, and Pd-HNC_{10}) were prepared with the addition of 1, 2, 5, and 10 mg of $Pd(OAc)_2$ to 20 mg of HNC, respectively. Note that for the Pd-HNC_{10} sample, the color of the supernatant remained virtually unchanged before and after thermal refluxing, suggesting saturated loading of Pd into the HNC matrix (Figure S1). The exact Pd contents in the samples were then quantitatively assessed by ICP-OES measurements (Table S1): 0.87 wt % for Pd-HNC_1, 1.75 wt % for Pd-HNC_2, 4.36 wt % for Pd-HNC_5, and 7.77 wt % for Pd-HNC_{10}. For the control sample PdNP/HNC where Pd nanoparticles were deposited onto the HNC surface by $NaBH_4$ reduction of $Pd(OAc)_2$, the palladium content was estimated to be 2.61 wt %.

The loading of Pd into the HNC matrix led to a marked change of the sample porosity. The inset to Figure 1c shows the N_2 sorption isotherms of HNC and Pd-HNC_{10}. For the HNC sample, one can see a sharp increase of the adsorbed N_2 quantity at low relative pressures, suggesting a substantial number of micropores. In fact, NLDFT fitting shows that the HNC sample was dominated with micropores (~1 nm), as evidenced in the pore-size distribution diagram (Figure 1c). Furthermore, in contrast to the porous carbon derived pyrolytically from solid ZIF-8 powders (without tannic acid etching) reported in the literature,[50] the HNC sample demonstrated a huge adsorption−desorption hysteresis loop and a range of mesopores between 2 and 10 nm. This suggests that HNC consisted of a hierarchical structure with mesopores and micropores (Figure S2)—a unique feature conducive to enhanced accessibility of the catalytic active sites on the carbon matrix and electrochemical mass transfer as compared to solid nitrogen-doped carbon (Figure S3).[23] Interestingly, after thermal refluxing with $Pd(OAc)_2$, the specific surface area, based on the BET method, was found to decrease markedly by about 80% from 410.21 $m^2 g^{-1}$ for HNC to only 85.39 $m^2 g^{-1}$ for Pd-HNC_{10}. In fact, from Figure 1c, one can see that micropores (~1 nm) disappeared almost completely from the pore size distribution plot, consistent with the impregnation of Pd species into the HNC matrix most likely by the N dopant/defect sites, and the fact that the hysteresis loop remained in the N_2 adsorption−desorption isotherm indicates that the Pd-HNC_{10} sample mainly contained mesopores (Figure S2).

https://dx.doi.org/10.1021/acsami.0c03415
ACS Appl. Mater. Interfaces 2020, 12, 17641−17650

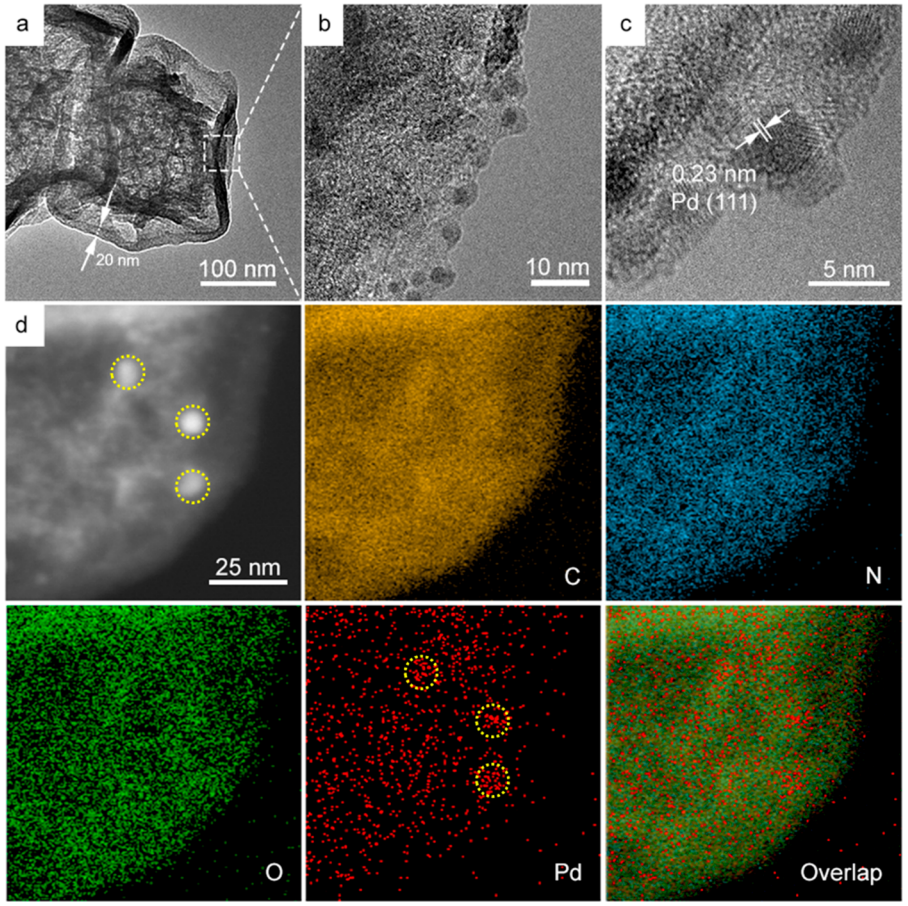

Figure 2. (a–c) Representative TEM images of Pd-HNC$_{10}$ at varied magnifications. (d) HAADF-STEM image of Pd-HNC$_{10}$ and the corresponding elemental maps of carbon, nitrogen, oxygen, palladium, and overlap. The few Pd nanoparticles are highlighted in dotted yellow circles.

The morphology of the Pd-HNC samples was then characterized by TEM measurements. From Figure 2a, the Pd-HNC$_{10}$ sample can be seen to display a cage-like structure with a diameter of around 200 nm and a shell thickness of ca. 20 nm. Similar hollow structures are produced with other Pd-HNC samples (Figure S4), and extensive mesoporosity can be seen in all samples. At higher magnifications (Figure 2b,c), one can see that the sample surface was also decorated with a few nanoparticles of ca. 3 nm in diameter, and the number of nanoparticles diminishes with decreasing loading of Pd(OAC)$_2$ in thermal refluxing—none can be found with Pd-HNC$_1$ (Figure S4). The nanoparticles display well-defined lattice fringes with a *d* spacing of 0.23 nm that can be ascribed to the (111) planes of fcc palladium,[53,54] and these Pd nanoparticles[55−57] can be seen to be partly encapsulated within a carbon shell. By contrast, no carbon encapsulation was observed for the palladium nanoparticles in PdNP/HNC (also ca. 3 nm in diameter), which clustered onto the HNC surface (Figure S5), with the {111} facets clearly identified in the fast Fourier transform (FFT) patterns.

Further structural details were obtained from high angle annular dark field scanning TEM (HAADF-STEM) measurements and the corresponding elemental mapping studies based on energy-dispersive X-ray (EDX) analysis (Figure 2d). One can see that (a) nitrogen (and oxygen) is distributed rather evenly over the entire carbon matrix, confirming successful nitrogen doping of the carbon skeletons, and (b) in addition to the few Pd nanoparticles (dotted yellow circles) a large number of palladium atomic species can also be seen to be homogeneously dispersed within the HNC matrix (Figure 2d and Figure S6).

Consistent results were obtained in XRD measurements. From Figure S7, both PdNP/HNC and Pd-HNC$_{10}$ samples can be seen to exhibit only a broad diffraction peak at 2θ = 39.5°, which can be ascribed to the (111) crystalline planes of fcc palladium (JCPDS no. 96-101-1105).[58] This diffraction feature was not observed with HNC alone or other Pd-HNC samples prepared at reduced Pd loadings, consistent with the results from TEM measurements (Figure 1 and Figure S4).

XPS measurements were then performed to examine the elemental composition and valence states of the samples. From the survey spectra in Figure S8, the elements of C, Pd, N, and O can be readily identified at 284, 338, 400, and 531 eV, respectively, for all Pd-HNC and PdNP/HNC samples, from which the Pd content was found to increase with the increasing feed ratio of Pd(OAc)$_2$: 3.55 wt % for Pd-HNC$_1$, 7.74 wt % for Pd-HNC$_2$, 6.58 wt % for Pd-HNC$_5$, and 17.48 wt % for Pd-HNC$_{10}$, in comparison to 9.88 wt % for PdNP/HNC (Table S2). One may note that these concentrations are markedly higher than those obtained by ICP-OES measurements (Table S1), suggesting that Pd was indeed predominantly situated and enriched on the HNC surface, as XPS probes only the surface layers of the samples. The high-resolution scans of the Pd 3d electrons are depicted in Figure 3a, where deconvolution can be seen to yield two doublets. The first pair (red peaks) at 335.8 and 341.1 eV can be attributed to the 3d$_{3/2}$ and 3d$_{5/2}$

https://dx.doi.org/10.1021/acsami.0c03415
ACS Appl. Mater. Interfaces 2020, 12, 17641−17650

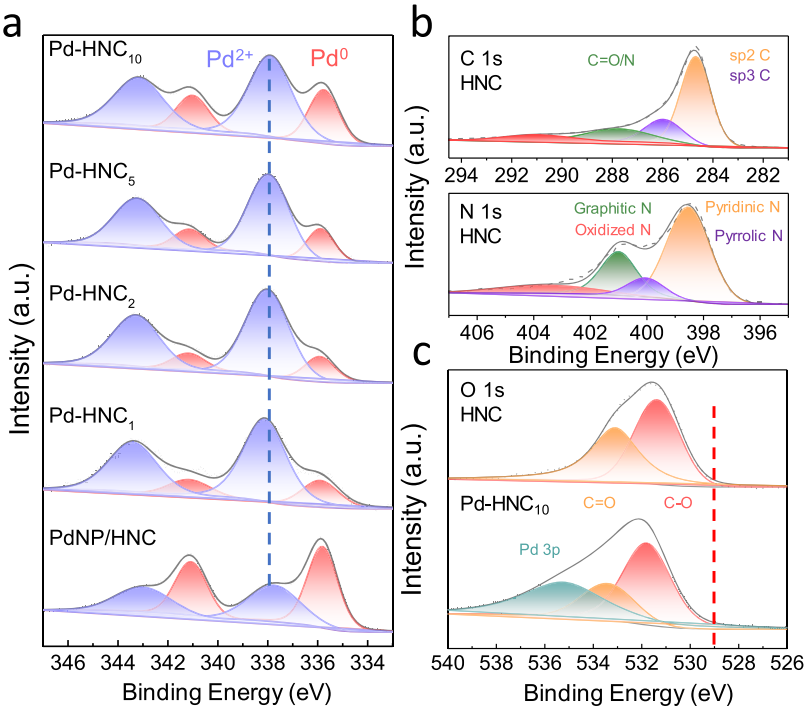

Figure 3. (a) High-resolution XPS spectra of the Pd 3d electrons of the Pd-HNC series and PdNP/HNC. (b) High-resolution XPS spectra of the C 1s (upper) and N 1s (bottom) electrons of HNC. (c) High-resolution XPS spectra of O 1s electrons of HNC and Pd-HNC$_{10}$. The red dashed line indicates the binding energy of the O 1s electrons in Pd−O. Solid curves are experimental data, and shaded peaks are deconvolution fits.

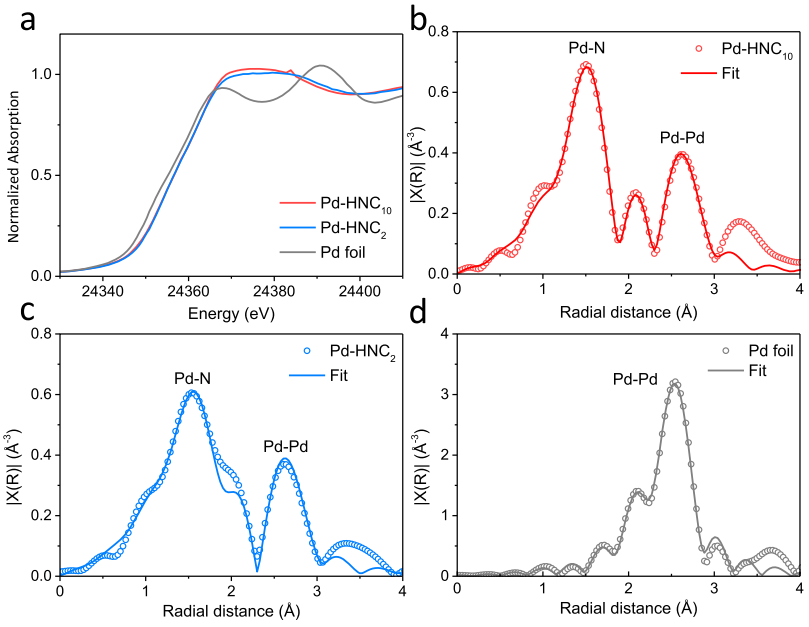

Figure 4. (a) Pd K-edge normalized XANES profiles of Pd-HNC$_{10}$, Pd-HNC$_2$, and Pd foil. Fourier transform EXAFS spectra of (b) Pd-HNC$_{10}$, (c) Pd-HNC$_2$, and (d) Pd foil. Symbols are experimental data, and solid curves are the fits.

electrons of metallic palladium, most likely due to the few nanoparticles observed in TEM measurements (Figure 2).[19,37,59,60] The other pair (purple peaks) appear at higher binding energies of 337.9 and 343.2 eV, comparable to those of Pd^{2+} species,[61,62] consistent with results from HAADF-STEM measurements (Figure 2d), which clearly showed atomic dispersion of Pd^{2+} species within the HNC matrix. It should be noted that the binding energies of Pd^{2+} in Pd-HNC are much higher than those of PdO (ca. 336.5 and 341.8 eV) but lower than those of Pd(OAC)$_2$ (ca. 338.5 and 343.8 eV),[19,61,63−65] suggesting that the Pd^{2+} species in Pd-HNC were unlikely due to the surface oxidation of Pd nanoparticles or excessive metal precursors. Moreover, based on the integrated peak areas, the atomic ratio of Pd^{2+}:Pd^0 in the samples can be seen to increase with decreasing Pd(OAC)$_2$ feed: at 5.6 for Pd-HNC$_1$, 4.5 for Pd-HNC$_2$, 3.5 for Pd-HNC$_5$, and 2.3 for Pd-HNC$_{10}$ (Table S2). That is, for the Pd-HNC series, the dominant species is Pd atomically dispersed within the HNC matrix. For

https://dx.doi.org/10.1021/acsami.0c03415
ACS Appl. Mater. Interfaces 2020, 12, 17641−17650

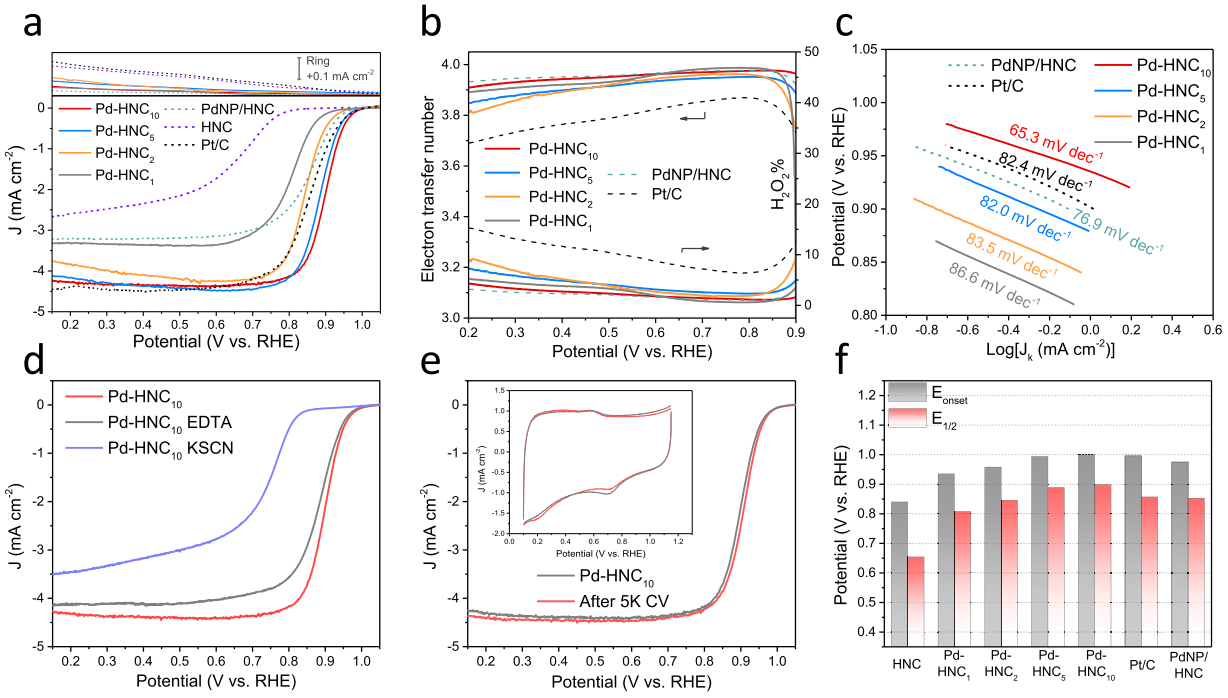

Figure 5. ORR performance of the Pd-HNC series in oxygen-saturated 0.1 M KOH. (a) Linear sweep voltammograms (LSVs) of Pd-HNC nanocomposites and control samples of HNC, PdNP/HNC, and Pt/C at the rotation rate of 1600 rpm. (b) The corresponding electron-transfer number (*n*, left *y*-axis), yield of H_2O_2 (%, right *y*-axis), and (c) Tafel plots with the slopes shown in mV dec^{-1}. (d) Poisoning test of Pd-HNC_{10} with EDTA and KSCN treatments. (e) Stability test of Pd-HNC_{10} for 5000 cycles in N_2-saturated 0.1 M KOH. Inset is the corresponding cyclic voltammograms at the scan rate of 50 mV s^{-1} before and after the stability test. (f) Comparison of E_{onset} and $E_{1/2}$ of the Pd-HNC series with those of HNC, PdNP/HNC, and Pt/C.

comparison, the Pd^{2+}:Pd^0 ratio is only 0.77 in PdNP/HNC, suggesting that nanoparticles are the major product together with a small number of atomic Pd species. Furthermore, in conjunction with the total Pd content obtained from ICP-OES measurements (Table S1), one can see that Pd-HNC_{10} possessed the highest loading of atomic Pd^{2+} species (5.42 wt %), which is drastically higher than those of Pd SACs reported in the literature (Table S3).

The C 1s and N 1s spectra of the HNC sample are shown in Figure 3b. In the C 1s spectrum, the major component is sp^2-hybridized C, which accounts for ca. 77 at. % of the sample, indicating effective carbonization of the ZIF-8 precursor by pyrolysis. In the N 1s spectrum, deconvolution yields four peaks at 398.5 eV for pyridinic N, 400.0 eV for pyrrolic N, 401.0 eV for graphitic N, and 402.8 eV for oxidized N; their contents are 4.63, 1.49, 1.58, and 1.40 at. %, respectively, corresponding to a total nitrogen dopant concentration of ca. 9.1 at. %. In the Pd-HNC samples, the Pd^{2+} species is most likely coordinated to the pyrrolic/pyridinic N. This argument is supported, in part, by the observation that no Pd−O peak (529 eV, red dashed line) can be resolved in the O 1s spectra (Figure 3c and Figure S9). However, it is difficult to resolve Pd−N in the N 1s spectra because the binding energy is close to those of pyrrolic/pyridinic N.[22]

Such structural details can be resolved in XAS measurements. Figure 4a depicts the Pd K-edge X-ray absorption near-edge structure (XANES) spectra of Pd-HNC_{10} and Pd-HNC_2, with a Pd foil as the reference. One can see that Pd-HNC_{10} and Pd-HNC_2 display very similar XANES profiles, suggesting similar Pd electronic environments. Yet the absorption edge can be seen to appear at a higher energy than that of the Pd foil, along with a higher peak intensity for the first peak following the edge, consistent with the existence of positively charged Pd species in the Pd-HNC samples, which was evidenced in TEM and XPS measurements (Figures 2 and 3). Furthermore, the flat postedge feature of Pd-HNC_{10} and Pd-HNC_2 within the range of 24370−24385 eV can be attributed to the combined contributions of Pd atomic species (which display a peak-like feature) and Pd nanoparticles (which display a valley-like feature).[33,66] Moreover, the postedge intensity of Pd-HNC_{10} (red curve) is slightly higher than that of Pd-HNC_2(blue curve), in good agreement with the higher concentration of Pd^{2+} species in Pd-HNC_{10}, as determined by XPS measurements (Table S2).

Further structural insights were obtained from analysis of the EXAFS spectra. From the Fourier transform EXAFS spectra in Figure 4b−d, one can see that the Pd foil displays a major peak at 2.54 Å arising from the Pd−Pd bond.[67] This peak is also visible in both Pd-HNC_{10} and Pd-HNC_2, consistent with the formation of Pd nanoparticles in the samples; however, a more prominent peak can be identified below 2 Å that most likely arose from Pd−O and/or Pd−N bonds with the carbon support.[68] Yet, as mentioned earlier, in the XPS measurements of the Pd 3d and O 1s electrons of Pd-HNC_{10} and Pd-HNC_2 (Figure 3a,c and Figure S9), no Pd−O species was found, indicating that this peak most likely arose from a Pd−N bonding interaction. Consistent results were obtained in EXAFS measurements, where no Pd−Pd bonds from Pd−O−Pd at ca. 3.0 Å can be resolved,[33,69] indicating the absence of PdO_x nanoclusters in the samples. From fitting of the spectral data (Figure 4b−d), the bond length can be calculated to be 2.004 Å for Pd−N and 2.797 Å for Pd−Pd in Pd-HNC_{10} (note that the peak positions may deviate from the true bond lengths due to the Fourier transform process, and EXAFS

https://dx.doi.org/10.1021/acsami.0c03415
ACS Appl. Mater. Interfaces 2020, 12, 17641−17650

fitting allows for the actual bond lengths in the samples to be calculated). The latter is slightly longer than that (2.741 Å) of the Pd foil. Yet the corresponding coordination numbers (CN) were found to be 3.4 for Pd−N and 2.2 for Pd−Pd in Pd-HNC$_{10}$. One can see that the latter is markedly smaller than that (12) of the Pd foil. This is because Pd single atoms are the predominant species in the Pd-HNC$_{10}$ sample.[56] Similar CN and bond lengths (Table S4) were obtained for Pd-HNC$_2$, suggesting a very similar bonding configuration of atomic Pd in the Pd-HNC samples, which is most likely in the form of PdN$_{3-4}$.

The ORR activity of the obtained samples was then assessed and compared by RRDE measurements in O$_2$-saturated 0.1 M KOH at the rotation rate of 1600 rpm and potential sweep rate of 10 mV s^{-1}. From the linear sweep voltammograms (LSV) in Figure 5a, all Pd-HNC samples can be seen to exhibit apparently enhanced electrocatalytic activity toward ORR, as compared to HNC alone, and the performance increases with increasing Pd loading in the sample. That is, Pd-HNC$_{10}$ stood out as the best ORR catalysts among the series, within the present experimental context. For instance, Pd-HNC$_1$ exhibited E_{onset} = +0.946 V and $E_{1/2}$ = +0.808 V, over 100 mV better than HNC alone, and both E_{onset} and $E_{1/2}$ further increased to +0.958 and +0.846 V for Pd-HNC$_2$, +0.994 and +0.889 V for Pd-HNC$_5$, and +1.00 and +0.898 V for Pd-HNC$_{10}$. For comparison, the E_{onset} and $E_{1/2}$ of the PdNP/HNC sample can be identified at +0.975 and +0.853 V, respectively, comparable to the performance of Pd-HNC$_2$ despite a higher Pd content (Table S1), suggesting that atomic Pd species in the Pd-HNC samples made dominant contributions to the ORR activity, with minor contributions from the nanoparticles. Notably, one can see that the Pd-HNC$_{10}$ even outperformed commercial 20 wt % Pt/C (E_{onset} = +0.996 V, $E_{1/2}$ = +0.857 V) and is also superior to leading Pd-based ORR catalysts reported recently in the literature (Table S5).

To further analyze the ORR kinetics, the number of electron transfers (n) was estimated by $n = \frac{4i_D}{i_D + i_R/N}$, where i_R and i_D are the ring current and disk current, respectively, and N is the collection efficiency of the ring electrode (0.40, Figure S10). From Figure 5b, one can see that the n number of the Pd-HNC$_{10}$ sample is over 3.97 at +0.85 V, even higher than that of Pt/C (3.84), indicating high selectivity toward the four-electron pathway of oxygen reduction. The Pd-HNC$_{10}$ also showed a very low H_2O_2% yield of 1.1% at +0.85 V, which was calculated by $H_2O_2\% = \frac{200i_R/N}{i_D + i_R/N}$, much lower than that of Pt/C (7.6%). In the Tafel plots (Figure 5c), Pd-HNC$_{10}$ exhibited the smallest slope of 65.3 mV dec^{-1}, in comparison to 76.9 mV dec^{-1} for PdNP/HNC, 83.5 mV dec^{-1} for Pd-HNC$_2$, and 82.4 mV dec^{-1} for Pt/C, implying efficient electron transfer to O$_2$ and splitting of the O−O bonds.[70]

The ORR activity of the Pd-HNC samples in acidic media was also assessed in O$_2$-saturated 0.1 M HClO$_4$ at the sweep rate of 10 mV s^{-1} and the rotation rate of 1600 rpm (Figure S11). The Pd-HNC$_{10}$ again showed the best activity among the series of samples with an E_{onset} of +0.912 V and an $E_{1/2}$ of +0.792 V.

To further distinguish the contributions of Pd nanoparticles and Pd atomic species to the ORR activity, electrochemical tests were performed in the presence of KSCN and EDTA as the poisoning agents. From Figure 5d, one can see that when the Pd-HNC$_{10}$ sample was treated with 10 mM EDTA in the 0.1 M KOH solution, the $E_{1/2}$ shifted negatively by 20 mV and the limiting current decreased by 8%. Yet upon the addition of 10 mM KSCN into the electrolyte, the $E_{1/2}$ shifted negatively by more than 200 mV and the limiting current diminished by over 1/3, and the overall performance resembled that of HNC alone. Note that SCN$^-$ readily adsorbed to and blocked both Pd nanoparticles and Pd−N sites, whereas EDTA poisoned predominantly the Pd−N species (Figure S12). The different poisoning effects by KSCN and EDTA suggest that both Pd nanoparticles and Pd−N moieties contributed to the ORR activity, with Pd−N being the dominant contributor.

The long-term durability of the Pd-HNC sample was then evaluated by prolonged potential cycling between +0.65 and +1.05 V at the potential sweep rate of 100 mV s^{-1}. As shown in Figure 5e, after 5000 cycles, the ORR activity of Pd-HNC$_{10}$ remained virtually invariant. Interestingly, from the cyclic voltammograms of Pd-HNC$_{10}$ before and after 5000 potential cycles (inset to Figure 5e), one can see that the cathodic peak of PdO$_x$ reduction became weakened after the stability test, indicating a partial loss of metallic palladium (mostly from the nanoparticles); yet the ORR activity was almost unaffected, further confirming that indeed the ORR activity was largely due to the Pd−N atomic species.

The contributions of Pd nanoparticles and single atoms to the ORR activity can also be differentiated by correlation of the ORR activity with the concentration of the various Pd species in the Pd-HNC samples. One can see from Figure 6 that if the

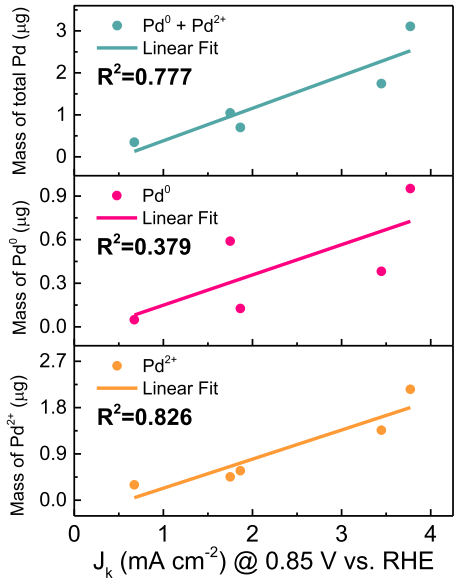

Figure 6. Linear correlation between the ORR kinetic current density (J_k at +0.85 V) and the mass of Pd^0, Pd^{2+}, or Pd^0 + Pd^{2+} of Pd-HNC.

activity was attributed to the total mass of Pd, the linear fit of the kinetic current density (i.e., specific activity, J_k) at +0.85 V vs the total mass of Pd (green line) is rather poor with an R^2 coefficient of only 0.777. Because results of XPS measurements showed the formation of both metallic Pd^0 and atomic Pd^{2+}, their contributions to the ORR activity were then analyzed and differentiated. When Pd^0 was assumed as the contributing source of the ORR activity, the correlation of J_k with the Pd^0 mass demonstrated a scatter plot with an even worse correlation coefficient of R^2 = 0.379. By contrast, when the

https://dx.doi.org/10.1021/acsami.0c03415
ACS Appl. Mater. Interfaces 2020, 12, 17641−17650

ORR activity was correlated to the mass of the Pd^{2+} species (Pd−N active sites), linear regression of the scatter plot showed a better R^2 of 0.826, suggesting that Pd^{2+} is indeed more likely the dominating species responsible for the ORR activity. This is consistent with results from the ORR poisoning test.

CONCLUSIONS

In this study, a facile procedure based on wet impregnation was developed, whereby Pd was atomically dispersed and enriched onto the surface of N-doped porous carbon cages derived from hollow ZIF-8 precursors. This was manifested in high-resolution TEM, XPS, and XAS measurements, where Pd was mostly involved in the formation of PdN_x moieties. Electrochemically, the obtained Pd-HNC samples exhibited markedly enhanced ORR activity in alkaline media as compared to the nanoparticle counterparts and the carbon cages alone, and the Pd-HNC_{10} sample, which corresponded to a saturated Pd loading, even outperformed Pt/C and leading Pd-based catalysts in the literature. The remarkable ORR performance was ascribed mostly to the atomic Pd species in the samples, which were predominantly enriched on the carbon support surface. Results from this study highlight the significance of metal single atom catalysts and their surface enrichments in ORR electrocatalysis. In addition, such a unique structural scaffold can be exploited for the embedment of a wide range of metal centers for diverse applications.

ASSOCIATED CONTENT

Supporting Information

The Supporting Information is available free of charge at https://pubs.acs.org/doi/10.1021/acsami.0c03415.

Additional experimental data and discussion (PDF)

AUTHOR INFORMATION

Corresponding Author

Shaowei Chen − *Department of Chemistry and Biochemistry, University of California, Santa Cruz, Santa Cruz, California 95064, United States;* orcid.org/0000-0002-3668-8551; Email: shaowei@ucsc.edu

Authors

Qiming Liu − *Department of Chemistry and Biochemistry, University of California, Santa Cruz, Santa Cruz, California 95064, United States;* orcid.org/0000-0001-5839-5453

Yi Peng − *Department of Chemistry and Biochemistry, University of California, Santa Cruz, Santa Cruz, California 95064, United States;* orcid.org/0000-0002-5319-1336

Qiaoxia Li − *Department of Chemistry and Biochemistry, University of California, Santa Cruz, Santa Cruz, California 95064, United States; Shanghai Key Laboratory of Materials Protection and Advanced Materials in Electric Power, College of Environmental and Chemical Engineering, Shanghai University of Electric Power, Shanghai 200090, China*

Ting He − *Department of Chemistry and Biochemistry, University of California, Santa Cruz, Santa Cruz, California 95064, United States; Hunan Provincial Key Laboratory of Chemical Power Sources, College of Chemistry and Chemical Engineering, Central South University, Changsha, Hunan 410083, China*

David Morris − *Department of Chemistry, Dalhousie University, Halifax, NS B3H 4R2, Canada*

Forrest Nichols − *Department of Chemistry and Biochemistry, University of California, Santa Cruz, Santa Cruz, California 95064, United States*

Rene Mercado − *Department of Chemistry and Biochemistry, University of California, Santa Cruz, Santa Cruz, California 95064, United States*

Peng Zhang − *Department of Chemistry, Dalhousie University, Halifax, NS B3H 4R2, Canada;* orcid.org/0000-0003-3603-0175

Complete contact information is available at: https://pubs.acs.org/10.1021/acsami.0c03415

Notes

The authors declare no competing financial interest.

ACKNOWLEDGMENTS

This work was supported in part by the National Science Foundation (CBET-1848841 and CHE-1900235). TEM, BET, and XPS work were performed at the National Center for Electron Microscopy and Molecular Foundry, Lawrence Berkeley National Laboratory, which is supported by the Office of Science, Office of Basic Energy Sciences, of the U.S. Department of Energy (DOE) under Contract DE-AC02-05CH11231 as part of a user project. The CLS@APS facilities (Sector 20-BM) at the Advanced Photon Source (APS) are supported by the US DOE, NSERC Canada, the University of Washington, the Canadian Light Source (CLS), and the APS. Use of the APS is supported by the DOE under Contract DE-AC02-06CH11357. The CLS is financially supported by NSERC Canada, CIHR, NRC, and the University of Saskatchewan.

REFERENCES

(1) Debe, M. K. Electrocatalyst Approaches and Challenges for Automotive Fuel Cells. *Nature* **2012**, *486*, 43−51.

(2) Seh, Z. W.; Kibsgaard, J.; Dickens, C. F.; Chorkendorff, I. B.; Norskov, J. K.; Jaramillo, T. F. Combining Theory and Experiment in Electrocatalysis: Insights into Materials Design. *Science* **2017**, *355*, No. eaad4998.

(3) Shao, M. H.; Chang, Q. W.; Dodelet, J. P.; Chenitz, R. Recent Advances in Electrocatalysts for Oxygen Reduction Reaction. *Chem. Rev.* **2016**, *116*, 3594−3657.

(4) Esposito, D. V.; Chen, J. G. G. Monolayer Platinum Supported on Tungsten Carbides as Low-Cost Electrocatalysts: Opportunities and Limitations. *Energy Environ. Sci.* **2011**, *4*, 3900−3912.

(5) Chen, C.; Kang, Y. J.; Huo, Z. Y.; Zhu, Z. W.; Huang, W. Y.; Xin, H. L. L.; Snyder, J. D.; Li, D. G.; Herron, J. A.; Mavrikakis, M.; Chi, M. F.; More, K. L.; Li, Y. D.; Markovic, N. M.; Somorjai, G. A.; Yang, P. D.; Stamenkovic, V. R. Highly Crystalline Multimetallic Nanoframes with Three-Dimensional Electrocatalytic Surfaces. *Science* **2014**, *343*, 1339−1343.

(6) Lopes, P. P.; Strmcnik, D.; Tripkovic, D.; Connell, J. G.; Stamenkovic, V.; Markovic, N. M. Relationships between Atomic Level Surface Structure and Stability/Activity of Platinum Surface Atoms in Aqueous Environments. *ACS Catal.* **2016**, *6*, 2536−2544.

(7) Stamenkovic, V. R.; Strmcnik, D.; Lopes, P. P.; Markovic, N. M. Energy and Fuels from Electrochemical Interfaces. *Nat. Mater.* **2017**, *16*, 57−69.

(8) Norskov, J. K.; Rossmeisl, J.; Logadottir, A.; Lindqvist, L.; Kitchin, J. R.; Bligaard, T.; Jonsson, H. Origin of the Overpotential for Oxygen Reduction at a Fuel-Cell Cathode. *J. Phys. Chem. B* **2004**, *108*, 17886−17892.

(9) Wang, D. L.; Xin, H. L. L.; Hovden, R.; Wang, H. S.; Yu, Y. C.; Muller, D. A.; DiSalvo, F. J.; Abruna, H. D. Structurally Ordered Intermetallic Platinum-Cobalt Core-Shell Nanoparticles with En-

hanced Activity and Stability as Oxygen Reduction Electrocatalysts. *Nat. Mater.* **2013**, *12*, 81−87.
(10) Cui, Z. M.; Chen, H.; Zhao, M. T.; DiSalvo, F. J. High-Performance Pd3pb Intermetallic Catalyst for Electrochemical Oxygen Reduction. *Nano Lett.* **2016**, *16*, 2560−2566.
(11) Xiong, Y.; Yang, Y.; Feng, X. R.; DiSalvo, F. J.; Abruna, H. D. A Strategy for Increasing the Efficiency of the Oxygen Reduction Reaction in Mn-Doped Cobalt Ferrites. *J. Am. Chem. Soc.* **2019**, *141*, 4412−4421.
(12) Jiang, J.; Ding, W.; Li, W.; Wei, Z. Freestanding Single-Atom-Layer Pd-Based Catalysts: Oriented Splitting of Energy Bands for Unique Stability and Activity. *Chem.* **2020**, *6*, 431−447.
(13) Jiang, G. M.; Zhu, H. Y.; Zhang, X.; Shen, B.; Wu, L. H.; Zhang, S.; Lu, G.; Wu, Z. B.; Sun, S. H. Core/Shell Face-Centered Tetragonal Fepd/Pd Nanoparticles as an Efficient Non-Pt Catalyst for the Oxygen Reduction Reaction. *ACS Nano* **2015**, *9*, 11014−11022.
(14) Wang, Y.; Yang, Y.; Jia, S. F.; Wang, X. M.; Lyu, K. J.; Peng, Y. Q.; Zheng, H.; Wei, X.; Ren, H.; Xiao, L.; Wang, J. B.; Muller, D. A.; Abruna, H. D.; Hwang, B. O. E.; Lu, J. T.; Zhuang, L. Synergistic Mn-Co Catalyst Outperforms Pt on High-Rate Oxygen Reduction for Alkaline Polymer Electrolyte Fuel Cells. *Nat. Commun.* **2019**, *10*, 1506.
(15) Peng, Y.; Lu, B. Z.; Wang, N.; Lu, J. E.; Li, C. H.; Ping, Y.; Chen, S. W. Oxygen Reduction Reaction Catalyzed by Black-Phosphorus-Supported Metal Nanoparticles: Impacts of Interfacial Charge Transfer. *ACS Appl. Mater. Interfaces* **2019**, *11*, 24707−24714.
(16) Deng, J.; Deng, D. H.; Bao, X. H. Robust Catalysis on 2d Materials Encapsulating Metals: Concept, Application, and Perspective. *Adv. Mater.* **2017**, *29*, 1606967.
(17) He, G. Q.; Song, Y.; Liu, K.; Walter, A.; Chen, S.; Chen, S. W. Oxygen Reduction Catalyzed by Platinum Nanoparticles Supported on Graphene Quantum Dots. *ACS Catal.* **2013**, *3*, 831−838.
(18) Zhu, Y. P.; Guo, C. X.; Zheng, Y.; Qiao, S. Z. Surface and Interface Engineering of Noble-Metal-Free Electrocatalysts for Efficient Energy Conversion Processes. *Acc. Chem. Res.* **2017**, *50*, 915−923.
(19) Arrigo, R.; Schuster, M. E.; Xie, Z. L.; Yi, Y. M.; Wowsnick, G.; Sun, L. L.; Hermann, K. E.; Friedrich, M.; Kast, P.; Havecker, M.; Knop-Gericke, A.; Schlogl, R. Nature of the N-Pd Interaction in Nitrogen-Doped Carbon Nanotube Catalysts. *ACS Catal.* **2015**, *5*, 2740−2753.
(20) Liu, J.; Jiao, M. G.; Lu, L. L.; Barkholtz, H. M.; Li, Y. P.; Wang, Y.; Jiang, L. H.; Wu, Z. J.; Liu, D. J.; Zhuang, L.; Ma, C.; Zeng, J.; Zhang, B. S.; Su, D. S.; Song, P.; Xing, W.; Xu, W. L.; Wang, Y.; Jiang, Z.; Sun, G. Q. High Performance Platinum Single Atom Electrocatalyst for Oxygen Reduction Reaction. *Nat. Commun.* **2017**, *8*, 15938.
(21) Fei, H. L.; Dong, J. C.; Feng, Y. X.; Allen, C. S.; Wan, C. Z.; Volosskiy, B.; Li, M. F.; Zhao, Z. P.; Wang, Y. L.; Sun, H. T.; An, P. F.; Chen, W. X.; Guo, Z. Y.; Lee, C.; Chen, D. L.; Shakir, I.; Liu, M. J.; Hu, T. D.; Li, Y. D.; Kirkland, A. I.; Duan, X. F.; Huang, Y. General Synthesis and Definitive Structural Identification of Mn4c4 Single-Atom Catalysts with Tunable Electrocatalytic Activities. *Nat. Catal.* **2018**, *1*, 63−72.
(22) Zhao, L.; Zhang, Y.; Huang, L. B.; Liu, X. Z.; Zhang, Q. H.; He, C.; Wu, Z. Y.; Zhang, L. J.; Wu, J. P.; Yang, W. L.; Gu, L.; Hu, J. S.; Wan, L. J. Cascade Anchoring Strategy for General Mass Production of High-Loading Single-Atomic Metal-Nitrogen Catalysts. *Nat. Commun.* **2019**, *10*, 1801995.
(23) Lee, S. H.; Kim, J.; Chung, D. Y.; Yoo, J. M.; Lee, H. S.; Kim, M. J.; Mun, B. S.; Kwon, S. G.; Sung, Y. E.; Hyeon, T. Design Principle of Fe-N-C Electrocatalysts: How to Optimize Multimodal Porous Structures? *J. Am. Chem. Soc.* **2019**, *141*, 2035−2045.
(24) Wan, X.; Liu, X. F.; Li, Y. C.; Yu, R. H.; Zheng, L. R.; Yan, W. S.; Wang, H.; Xu, M.; Shui, J. L. Fe-N-C Electrocatalyst with Dense Active Sites and Efficient Mass Transport for High-Performance Proton Exchange Membrane Fuel Cells. *Nat. Catal.* **2019**, *2*, 259−268.
(25) He, T.; Zhang, Y. Q.; Chen, Y.; Zhang, Z. Z.; Wang, H. Y.; Hu, Y. F.; Liu, M.; Pao, C. W.; Chen, J. L.; Chang, L. Y.; Sun, Z. F.; Xiang, J.; Zhang, Y.; Chen, S. W. Single Iron Atoms Stabilized by Microporous Defects of Biomass-Derived Carbon Aerogels as High-Performance Cathode Electrocatalysts for Aluminum-Air Batteries. *J. Mater. Chem. A* **2019**, *7*, 20840−20846.
(26) Ye, Y. F.; Cai, F.; Li, H. B.; Wu, H. H.; Wang, G. X.; Li, Y. S.; Miao, S.; Xie, S. H.; Si, R.; Wang, J.; Bao, X. H. Surface Functionalization of Zif-8 with Ammonium Ferric Citrate toward High Exposure of Fe-N Active Sites for Efficient Oxygen and Carbon Dioxide Electroreduction. *Nano Energy* **2017**, *38*, 281−289.
(27) Yin, P. Q.; Yao, T.; Wu, Y.; Zheng, L. R.; Lin, Y.; Liu, W.; Ju, H. X.; Zhu, J. F.; Hong, X.; Deng, Z. X.; Zhou, G.; Wei, S. Q.; Li, Y. D. Single Cobalt Atoms with Precise N-Coordination as Superior Oxygen Reduction Reaction Catalysts. *Angew. Chem., Int. Ed.* **2016**, *55*, 10800−10805.
(28) Wu, H. H.; Li, H. B.; Zhao, X. F.; Liu, Q. F.; Wang, J.; Xiao, J. P.; Xie, S. H.; Si, R.; Yang, F.; Miao, S.; Guo, X. G.; Wang, G. X.; Bao, X. H. Highly Doped and Exposed Cu(I)-N Active Sites within Graphene Towards Efficient Oxygen Reduction for Zinc-Air Batteries. *Energy Environ. Sci.* **2016**, *9*, 3736−3745.
(29) Yang, Z. K.; Chen, B. X.; Chen, W. X.; Qu, Y. T.; Zhou, F. Y.; Zhao, C. M.; Xu, Q.; Zhang, Q. H.; Duan, X. Z.; Wu, Y. Directly Transforming Copper (I) Oxide Bulk into Isolated Single-Atom Copper Sites Catalyst through Gas-Transport Approach. *Nat. Commun.* **2019**, *10*, 3734.
(30) Lu, B. Z.; Smart, T. J.; Qin, D. D.; Lu, J. E.; Wang, N.; Chen, L. M.; Peng, Y.; Ping, Y.; Chen, S. W. Nitrogen and Iron-Codoped Carbon Hollow Nanotubules as High-Performance Catalysts toward Oxygen Reduction Reaction: A Combined Experimental and Theoretical Study. *Chem. Mater.* **2017**, *29*, 5617−5628.
(31) Zhang, C. H.; Sha, J. W.; Fei, H. L.; Liu, M. J.; Yazdi, S.; Zhang, J. B.; Zhong, Q. F.; Zou, X. L.; Zhao, N. Q.; Yu, H. S.; Jiang, Z.; Ringe, E.; Yakobson, B. I.; Dong, J. C.; Chen, D. L.; Tour, J. M. Single-Atomic Ruthenium Catalytic Sites on Nitrogen-Doped Graphene for Oxygen Reduction Reaction in Acidic Medium. *ACS Nano* **2017**, *11*, 6930−6941.
(32) Zhou, S. Q.; Shang, L.; Zhao, Y. X.; Shi, R.; Waterhouse, G. I. N.; Huang, Y. C.; Zheng, L. R.; Zhang, T. R. Pd Single-Atom Catalysts on Nitrogen-Doped Graphene for the Highly Selective Photothermal Hydrogenation of Acetylene to Ethylene. *Adv. Mater.* **2019**, *31*, 1900509.
(33) Wei, S. J.; Li, A.; Liu, J. C.; Li, Z.; Chen, W. X.; Gong, Y.; Zhang, Q. H.; Cheong, W. C.; Wang, Y.; Zheng, L. R.; Xiao, H.; Chen, C.; Wang, D. S.; Peng, Q.; Gu, L.; Han, X. D.; Li, J.; Li, Y. D. Direct Observation of Noble Metal Nanoparticles Transforming to Thermally Stable Single Atoms. *Nat. Nanotechnol.* **2018**, *13*, 856−861.
(34) Malko, D.; Kucernak, A.; Lopes, T. In Situ Electrochemical Quantification of Active Sites in Fe-N/C Non-Precious Metal Catalysts. *Nat. Commun.* **2016**, *7*, 13285.
(35) Peng, Y.; Lu, B. Z.; Chen, S. W. Carbon-Supported Single Atom Catalysts for Electrochemical Energy Conversion and Storage. *Adv. Mater.* **2018**, *30*, 1801995.
(36) Podyacheva, O. Y.; Bulushev, D. A.; Suboch, A. N.; Svintsitskiy, D. A.; Lisitsyn, A. S.; Modin, E.; Chuvilin, A.; Gerasimov, E. Y.; Sobolev, V. I.; Parmon, V. N. Highly Stable Single-Atom Catalyst with Ionic Pd Active Sites Supported on N-Doped Carbon Nanotubes for Formic Acid Decomposition. *ChemSusChem* **2018**, *11*, 3724−3727.
(37) Bulushev, D. A.; Zacharska, M.; Shlyakhova, E. V.; Chuvilin, A. L.; Guo, Y. N.; Beloshapkin, S.; Okotrub, A. V.; Bulusheva, L. G. Single Isolated Pd2+ Cations Supported on N-Doped Carbon as Active Sites for Hydrogen Production from Formic Acid Decomposition. *ACS Catal.* **2016**, *6*, 681−691.
(38) Passaponti, M.; Savastano, M.; Clares, M. P.; Inclan, M.; Lavacchi, A.; Bianchi, A.; Garcia-Espana, E.; Innocenti, M. Mwcnts-Supported Pd(Ii) Complexes with High Catalytic Efficiency in Oxygen Reduction Reaction in Alkaline Media. *Inorg. Chem.* **2018**, *57*, 14484−14488.

https://dx.doi.org/10.1021/acsami.0c03415
ACS Appl. Mater. Interfaces 2020, 12, 17641−17650

(39) Xiang, W. K.; Zhao, Y. H.; Jiang, Z.; Li, X. P.; Zhang, H.; Sun, Y.; Ning, Z. J.; Du, F. P.; Gao, P.; Qian, J.; Kato, K.; Yamauchi, M.; Sun, Y. H. Palladium Single Atoms Supported by Interwoven Carbon Nanotube and Manganese Oxide Nanowire Networks for Enhanced Electrocatalysis. *J. Mater. Chem. A* **2018**, *6*, 23366−23377.
(40) Zhu, Y. L.; Zhou, W.; Chen, Y. B.; Yu, J.; Xu, X. M.; Su, C.; Tade, M. O.; Shao, Z. P. Boosting Oxygen Reduction Reaction Activity of Palladium by Stabilizing Its Unusual Oxidation States in Perovskite. *Chem. Mater.* **2015**, *27*, 3048−3054.
(41) Peng, Y.; Lu, B. Z.; Chen, L. M.; Wang, N.; Lu, J. E.; Ping, Y.; Chen, S. W. Hydrogen Evolution Reaction Catalyzed by Ruthenium Ion-Complexed Graphitic Carbon Nitride Nanosheets. *J. Mater. Chem. A* **2017**, *5*, 18261−18269.
(42) Peng, Y.; Pan, W. Z.; Wang, N.; Lu, J. E.; Chen, S. W. Ruthenium Ion-Complexed Graphitic Carbon Nitride Nanosheets Supported on Reduced Graphene Oxide as High-Performance Catalysts for Electrochemical Hydrogen Evolution. *ChemSusChem* **2018**, *11*, 130−136.
(43) Zheng, F. C.; Yang, Y.; Chen, Q. W. High Lithium Anodic Performance of Highly Nitrogen-Doped Porous Carbon Prepared from a Metal-Organic Framework. *Nat. Commun.* **2014**, *5*, 5261.
(44) Zhang, Z. Q.; Chen, Y. G.; Zhou, L. Q.; Chen, C.; Han, Z.; Zhang, B. S.; Wu, Q.; Yang, L. J.; Du, L. Y.; Bu, Y. F.; Wang, P.; Wang, X. Z.; Yang, H.; Hu, Z. The Simplest Construction of Single-Site Catalysts by the Synergism of Micropore Trapping and Nitrogen Anchoring. *Nat. Commun.* **2019**, *10*, 1657.
(45) Yang, J.; Qiu, Z. Y.; Zhao, C. M.; Wei, W. C.; Chen, W. X.; Li, Z. J.; Qu, Y. T.; Dong, J. C.; Luo, J.; Li, Z. Y.; Wu, Y. In Situ Thermal Atomization to Convert Supported Nickel Nanoparticles into Surface-Bound Nickel Single-Atom Catalysts. *Angew. Chem., Int. Ed.* **2018**, *57*, 14095−14100.
(46) Ravel, B.; Newville, M. Athena, Artemis, Hephaestus: Data Analysis for X-Ray Absorption Spectroscopy Using Ifeffit. *J. Synchrotron Radiat.* **2005**, *12*, 537−541.
(47) Yang, Q. H.; Yang, C. C.; Lin, C. H.; Jiang, H. L. Metal-Organic-Framework-Derived Hollow N-Doped Porous Carbon with Ultrahigh Concentrations of Single Zn Atoms for Efficient Carbon Dioxide Conversion. *Angew. Chem., Int. Ed.* **2019**, *58*, 3511−3515.
(48) Hu, M.; Ju, Y.; Liang, K.; Suma, T.; Cui, J. W.; Caruso, F. Void Engineering in Metal-Organic Frameworks Via Synergistic Etching and Surface Functionalization. *Adv. Funct. Mater.* **2016**, *26*, 5827−5834.
(49) Liu, T.; Liu, W. L.; Zhang, M. K.; Yu, W. Y.; Gao, F.; Li, C. X.; Wang, S. B.; Feng, J.; Zhang, X. Z. Ferrous-Supply-Regeneration Nanoengineering for Cancer-Cell-Specific Ferroptosis in Combination with Imaging-Guided Photodynamic Therapy. *ACS Nano* **2018**, *12*, 12181−12192.
(50) Zhang, W.; Jiang, X. F.; Zhao, Y. Y.; Carne-Sanchez, A.; Malgras, V.; Kim, J.; Kim, J. H.; Wang, S. B.; Liu, J.; Jiang, J. S.; Yamauchi, Y.; Hu, M. Hollow Carbon Nanobubbles: Monocrystalline Mof Nanobubbles and Their Pyrolysis. *Chem. Sci.* **2017**, *8*, 3538−3546.
(51) Choi, S.; Oh, M. Well-Arranged and Confined Incorporation of Pdco Nanoparticles within a Hollow and Porous Metal-Organic Framework for Superior Catalytic Activity. *Angew. Chem., Int. Ed.* **2019**, *58*, 866−871.
(52) Zhang, F.; Wei, Y. Y.; Wu, X. T.; Jiang, H. Y.; Wang, W.; Li, H. X. Hollow Zeolitic Imidazolate Framework Nanospheres as Highly Efficient Cooperative Catalysts for [3 + 3] Cycloaddition Reactions. *J. Am. Chem. Soc.* **2014**, *136*, 13963−13966.
(53) Deming, C. P.; Mercado, R.; Lu, J. E.; Gadiraju, V.; Khan, M.; Chen, S. W. Oxygen Electroreduction Catalyzed by Palladium Nanoparticles Supported on Nitrogen-Doped Graphene Quantum Dots: Impacts of Nitrogen Dopants. *ACS Sustainable Chem. Eng.* **2016**, *4*, 6580−6589.
(54) Mazumder, V.; Sun, S. Oleylamine-Mediated Synthesis of Pd Nanoparticles for Catalytic Formic Acid Oxidation. *J. Am. Chem. Soc.* **2009**, *131*, 4588−4589.
(55) Ju, J.; Chen, W. In Situ Growth of Surfactant-Free Gold Nanoparticles on Nitrogen-Doped Graphene Quantum Dots for Electrochemical Detection of Hydrogen Peroxide in Biological Environments. *Anal. Chem.* **2015**, *87*, 1903−1910.
(56) Huang, F.; Deng, Y. C.; Chen, Y. L.; Cai, X. B.; Peng, M.; Jia, Z. M.; Ren, P. J.; Xiao, D. Q.; Wen, X. D.; Wang, N.; Liu, H. Y.; Ma, D. Atomically Dispersed Pd on Nanodiamond/Graphene Hybrid for Selective Hydrogenation of Acetylene. *J. Am. Chem. Soc.* **2018**, *140*, 13142−13146.
(57) Radkevich, V. Z.; Senko, T. L.; Wilson, K.; Grishenko, L. M.; Zaderko, A. N.; Diyuk, V. Y. The Influence of Surface Functionalization of Activated Carbon on Palladium Dispersion and Catalytic Activity in Hydrogen Oxidation. *Appl. Catal., A* **2008**, *335*, 241−251.
(58) Yang, J.; Tian, C. G.; Wang, L.; Fu, H. G. An Effective Strategy for Small-Sized and Highly-Dispersed Palladium Nanoparticles Supported on Graphene with Excellent Performance for Formic Acid Oxidation. *J. Mater. Chem.* **2011**, *21*, 3384−3390.
(59) Zacharska, M.; Bulusheva, L. G.; Lisitsyn, A. S.; Beloshapkin, S.; Guo, Y. N.; Chuvilin, A. L.; Shlyakhova, E. V.; Podyacheva, O. Y.; Leahy, J. J.; Okotrub, A. V.; Bulushev, D. A. Factors Influencing the Performance of Pd/C Catalysts in the Green Production of Hydrogen from Formic Acid. *ChemSusChem* **2017**, *10*, 720−730.
(60) Wang, F. N.; Xu, J. M.; Shao, X. Z.; Su, X.; Huang, Y. Q.; Zhang, T. Palladium on Nitrogen-Doped Mesoporous Carbon: A Bifunctional Catalyst for Formate-Based, Carbon-Neutral Hydrogen Storage. *ChemSusChem* **2016**, *9*, 246−251.
(61) Ding, S. Y.; Gao, J.; Wang, Q.; Zhang, Y.; Song, W. G.; Su, C. Y.; Wang, W. Construction of Covalent Organic Framework for Catalysis: Pd/Cof-Lzu1 in Suzuki-Miyaura Coupling Reaction. *J. Am. Chem. Soc.* **2011**, *133*, 19816−19822.
(62) Li, L. Y.; Zhao, H. X.; Wang, J. Y.; Wang, R. H. Facile Fabrication of Ultrafine Palladium Nanoparticles with Size- and Location-Control in Click-Based Porous Organic Polymers. *ACS Nano* **2014**, *8*, 5352−5364.
(63) Gabasch, H.; Unterberger, W.; Hayek, K.; Klotzer, B.; Kresse, G.; Klein, C.; Schmid, M.; Varga, P. Growth and Decay of the Pd(111)-Pd5o4 Surface Oxide: Pressure-Dependent Kinetics and Structural Aspects. *Surf. Sci.* **2006**, *600*, 205−218.
(64) Zemlyanov, D.; Aszalos-Kiss, B.; Kleimenov, E.; Teschner, D.; Zafeiratos, S.; Havecker, M.; Knop-Gericke, A.; Schlogl, R.; Gabasch, H.; Unterberger, W.; Hayek, K.; Klödtzer, B. In Situ Xps Study of Pd(111) Oxidation. Part 1:2d Oxide Formation in 10(−3) Mbar O-2. *Surf. Sci.* **2006**, *600*, 983−994.
(65) Gabasch, H.; Unterberger, W.; Hayek, K.; Klotzer, B.; Kleimenov, E.; Teschner, D.; Zafeiratos, S.; Havecker, M.; Knop-Gericke, A.; Schlogl, R.; Han, J. Y.; Ribeiro, F. H.; Aszalos-Kiss, B.; Curtin, T.; Zemlyanov, D. In Situ Xps Study of Pd(111) Oxidation at Elevated Pressure, Part 2: Palladium Oxidation in the 10(−1) Mbar Range. *Surf. Sci.* **2006**, *600*, 2980−2989.
(66) Lu, B. Z.; Guo, L.; Wu, F.; Peng, Y.; Lu, J. E.; Smart, T. J.; Wang, N.; Finfrock, Y. Z.; Morris, D.; Zhang, P.; Li, N.; Gao, P.; Ping, Y.; Chen, S. W. Ruthenium Atomically Dispersed in Carbon Outperforms Platinum toward Hydrogen Evolution in Alkaline Media. *Nat. Commun.* **2019**, *10*, 631.
(67) Kodre, A.; Arcon, I.; Batista, J.; Pintar, A. Exafs Analysis of Pd Atomic Clusters. *J. Synchrotron Radiat.* **1999**, *6*, 458−459.
(68) Koh, K.; Jeon, M.; Chevrier, D. M.; Zhang, P.; Yoon, C. W.; Asefa, T. Novel Nanoporous N-Doped Carbon-Supported Ultrasmall Pd Nanoparticles: Efficient Catalysts for Hydrogen Storage and Release. *Appl. Catal., B* **2017**, *203*, 820−828.
(69) Huang, W. X.; Zhang, S. R.; Tang, Y.; Li, Y. T.; Nguyen, L.; Li, Y. Y.; Shan, J. J.; Xiao, D. Q.; Gagne, R.; Frenkel, A. I.; Tao, F. Low-Temperature Transformation of Methane to Methanol on Pd1o4 Single Sites Anchored on the Internal Surface of Microporous Silicate. *Angew. Chem., Int. Ed.* **2016**, *55*, 13441−13445.
(70) Chlistunoff, J. Rrde and Voltammetric Study of Orr on Pyrolyzed Fe/Polyaniline Catalyst. On the Origins of Variable Tafel Slopes. *J. Phys. Chem. C* **2011**, *115*, 6496−6507.

https://dx.doi.org/10.1021/acsami.0c03415
ACS Appl. Mater. Interfaces 2020, 12, 17641−17650